metals

MDPI

Article

Corrosion Protection of Steel by NO_3^- and NO_2^- Intercalated Mg-Al Layered Double Hydroxides in Simulated Pore Solutions of Alkali-Activated Slag

Minxuan Zhong, Jinxia Xu *, Yiyang Jiang and You Wu

College of Civil and Transportation Engineering, Hohai University, Nanjing 210098, China
* Correspondence: xujinxia@hhu.edu.cn

Abstract: This paper aims to perform a comparative investigation on the corrosion protection of steel in the simulated pore solutions of alkali-activated slag (SH) by NO_3^- and NO_2^- intercalated Mg-Al layered double hydroxides (MAL) which were fabricated by the calcination rehydration method. The corrosion potential, electrochemical impedance spectroscopy, potentiodynamic polarization and corrosion condition of steel were measured. Furthermore, changes in the microstructures of NO_3^- intercalated MAL (MAL-N3) and NO_2^- intercalated MAL (MAL-N2) before and after the adsorption of chloride ion were observed by X-ray diffraction and Fourier transform infrared spectroscopy. The results show that compared to the simulated concrete pore solution (OPCH), MAL-N3 and MAL-N2 exhibit lower chloride adsorption capacities and better corrosion inhibition effects in SH. The chloride adsorption capacity of MAL-N2 is lower compared with that of MAL-N3 due to the different volumes of intercalated anions. In contrast, MAL-N2 presents superior corrosion inhibition than MAL-N3. Furthermore, the decreases in $[OH^-]$ in SH due to the additions of MAL-N3 and MAL-N2 are more prominent than those in OPCH. The different synergistic effects due to the competitive anion-exchanges in the interlayers of NO_3^- and NO_2^- intercalated MAL in the two solutions contribute to the above effects.

Keywords: Mg-Al layered double hydroxides; simulated pore solutions of alkali-activated slag; steel corrosion; inhibition effect

Citation: Zhong, M.; Xu, J.; Jiang, Y.; Wu, Y. Corrosion Protection of Steel by NO_3^- and NO_2^- Intercalated Mg-Al Layered Double Hydroxides in Simulated Pore Solutions of Alkali-Activated Slag. *Metals* **2024**, *14*, 111. https://doi.org/10.3390/met14010111

Academic Editor: Petros E. Tsakiridis

Received: 25 December 2023
Revised: 9 January 2024
Accepted: 11 January 2024
Published: 17 January 2024

1. Introduction

The production of ordinary Portland cement (OPC) emits 3.2 G tons of carbon dioxide per year, which accounts for about 8% of total greenhouse gas emissions [1]. Owing to concern about extensive carbon dioxide emission related to the manufacture of OPC, the pursuit of low-carbon cementitious materials has received much attraction. Alkali-activated materials (AAMs) are promising candidates which are manufactured by the chemical reaction of alkaline activator and solid aluminosilicate materials [2]. Ground granulated blast furnace slag (GGBFS), a by-product of iron manufacturing, is one of the most commonly used aluminosilicate materials that can be alkali activated to produce a cementitious material named alkali-activated slag (AAS) [3]. Furthermore, alkali-activated slag (AAS) can achieve comparable or even stronger mechanical properties relative to OPC and superior fire and chemical resistance [4]. As a result, the utilization of AAS to replace OPC as a cementitious material providing strength to concrete has become increasingly popular in recent years.

It is well known that chloride-induced corrosion of steel reinforcement is one of the main causes of decreased durability in reinforced concrete in the marine environment [5]. Owing to the porous structure of concrete, aggressive chloride ions from a marine environment will penetrate into concrete. When the concentration of chloride reaches the threshold level, the passive film on the steel surface will be broken and steel corrosion will be initiated [6]. Compared to OPC, AAS generally exhibits a denser structure and

a higher chloride-binding capacity, making it more difficult for the chloride to penetrate and delaying the initiation of steel corrosion [7]. Furthermore, the passive film on the steel surface in AAS is more protective than that in OPC based on electrochemical measurements [8]. The threshold Cl^-/OH^- value for steel pitting corrosion initiation in AAS concrete is higher compared with OPC concrete [7]. These properties make AAS more suitable for real application in marine environments. Despite this, long-term exposure to severe marine environments inevitably results in the onset of steel corrosion in AAS. To assure the long-term performance and further promote the real application of AAS in marine environments, it is necessary to investigate the additional corrosion prevention measures of steel in AAS.

Layered double hydroxides (LDHs) are a class of anionic clays for which the chemical formula is $[M^{2+}_{1-x}M^{3+}_{x}(OH)_2]^{x+}(A^{n-})_{x/n}\cdot yH_2O$. The principal layer of LDHs is composed of divalent metal cations M^{2+} and trivalent metal cations M^{3+} [9]. Some of the divalent metal cations contained in the principal layer are substituted by trivalent metal cations which make the layer positively charged. To achieve the electrical neutrality of LDHs, the anions A^{n-} are adsorbed into the interlayer by electrostatic attraction [10]. This force is so weak that the interlayered anions can be replaced with other anions that are more easily inserted into the gallery of LDHs. Herein, LDHs and modified LDHs with inhibitive anions are favorable for application as chloride adsorbents and corrosion inhibitors in OPC concrete by means of the interlayered anion exchange. H. Tatematsu et al. used mortars containing LDHs-NO_2 to repair reinforced concrete structures and found that the half-cell potential of the rebar moved positively by about 150 mV and most of the free chloride ions in the mortar were adsorbed [11]. Z. H. Shui et al. concluded that LDHs are significantly helpful for the paste to fix chloride and prevent the penetration of chloride into the concrete [12]. Jian Geng et al. observed that LDHs in cement could significantly adsorb chloride ions at 20~38 °C and contributed to forming Friedel's salt [13]. Xu J. et al. synthesized LDHs-NO_2 by the co-deposition method and claimed that LDHs-NO_2 could significantly adsorb chloride ions in the simulated concrete pore solution and possessed good corrosion inhibition for steel [14]. All the above works clearly demonstrate the excellent chloride adsorption and corrosion inhibition effects of LDHs and modified LDHs in OPC concrete.

Although much work on the application of LDHs in OPC concrete has been done, no special investigation on the influence of added LDHs on the chloride-induced corrosion of steel in AAS concrete has been performed. In fact, it was assumed that LDHs are one of the reaction products in AAS and are mainly responsible for the improved chloride binding of AAS [15]. Tao Liu et al. found that added LDHs-NO_3 can significantly adsorb chlorides in alkali-activated fly ash and slag blends [16]. However, the chemistry of the concrete pore solution in AAS is quite different from that of OPC. Furthermore, the alkalinity level of AAS is relatively higher compared with OPC [7]. Xu J. et al. found that LDHs had a pH buffering ability in concrete pore solution, and the alkalinity of the pore solution remarkably affected the corrosion inhibition effect of LDHs due to the competitive anion exchange in the gallery of LDHs [17]. All these results reveal that there are different corrosion inhibition behaviors of added LDHs in AAS and OPC concretes. Accordingly, it is necessary to study the corrosion inhibition effects of LDHs and modified LDHs with inhibitive anions on steel in AAS concrete.

This paper aims to perform a comparative investigation on the corrosion protection of steel in simulated pore solutions of AAS by NO_3^- and NO_2^- intercalated Mg-Al layered double hydroxides (MAL) which were fabricated by the calcination rehydration method. The corrosion potential (E_{corr}), electrochemical impedance spectroscopy (EIS), potentiodynamic polarization (PDP) and optical microscopy (OM) of steel were measured. The microstructure changes of NO_3^- intercalated MAL (MAL-N3) and NO_2^- intercalated MAL (MAL-N2) before and after chloride adsorption were observed by X-ray diffraction (XRD) and Fourier transform infrared spectroscopy (FT-IR).

2. Experimental Section

2.1. Materials

The reagents used in this study, such as $Mg_4Al_2(OH)_{12}CO_3{\cdot}mH_2O$ (MAL-C), $NaNO_3$, $NaNO_2$, NaCl and NaOH, were analytically pure. MAL-C(containing 33.0 ± 1 wt.% MgO, 22.0 ± 1 wt% Al_2O_3) was purchased from Beijing University of Chemical Technology. and other reagents were purchased from Kelong company. The water used was boiled deionized water. The apparent density of P·O 42.5 cement purchased from Hailuo company was 3100 kg/m^3 and its specific surface area was 350 m^2/kg. Meanwhile, the apparent density and specific surface area of granulated blast furnace slag (GGBFS) purchased from Henan province in China were 3100 kg/m^3 and 429 m^2/kg, respectively. The grade of granulated blast furnace slag used was S95 and the oxide compositions of cement and slag are listed in Table 1. The applied alkali activator was NaOH. The steel used to perform the corrosion test was mild steel of which the chemical composition was 97.56% Fe, 0.23% C, 0.31% Si, 0.63% Mn and 0.005% S.

Table 1. The oxide compositions of cement and slag (wt.%).

Materials	CaO	SiO_2	Al_2O_3	SO_3	Fe_2O_3	MgO	Na_2O	K_2O	LOI [a]
Cement	57.27	24.99	9.32	0.98	3.11	0.86	1.06	1.05	2.06
Slag	34.00	34.50	17.70	1.64	1.03	6.01	1.14	0.92	0.84

[a] LOI is Loss on Ignition.

2.2. Methods

2.2.1. Preparation of MAL

The calcination rehydration method was adopted to prepare MAL-N3 and MAL-N2 [18]. Commercial MAL-C was calcined in a Muffle furnace at 500 °C for 5 h and the resultant powder was denoted as MAL-0. Then, MAL-0 and $NaNO_3$ or $NaNO_2$ with a molar ratio of 1:3 were poured into a flask containing 100 mL boiled deionized water (solid to liquid ratio = 1:10) with magnetic stirring under N_2 atmosphere. The flask was put in the water bath at a temperature of 90 °C for 5 h. Subsequently, the resultant slurry was centrifuged and the white precipitate was obtained. The precipitate was washed and then dried out under vacuum at 70 °C for 24 h. The resultant powder was ground to obtain ultimate products of MAL-N3 or MAL-N2 with a particle diameter below 0.25 mm.

2.2.2. Preparation of Simulated Pore Solution of Alkali-Activated Slag

Quantities of 1000 g slag, 1985 mL deionized water and 65 g NaOH (Na_2O wt.% = 5 wt.% slag mass) were added to a plastic bucket and continuously stirred for 24 h [19]. The mixture was sealed and stored for 28 d. After this, the solid at the bottom was broken into a fine powder and the powder was stirred with the original solution in the bucket for 24 h. Then, the simulated pore solution of AAS concrete (denoted as SH) was obtained by filtering the suspension. Similarly, the simulated pore solution of OPC concrete (denoted as OPCH) was also prepared to make a comparison.

2.2.3. Chloride Adsorption Equilibrium Isotherms

A series of OPCH and SH containing different concentrations of chloride (2, 5, 10, 20, 40, 80 and 160 mmol/L) were prepared. Then, 1 g MAL-N3 and 1 g MAL-N2 were, respectively, added to 100 mL OPCH and SH. Next, the containers containing OPCH and SH were put in an ultrasonic cleaner to disperse MAL (MAL-N3 and MAL-N2) for 30 min and stored at room temperature for 24 h. After centrifugation, the chloride content in the supernatant was measured by potentiometric titration using 0.01 mol/L $AgNO_3$. The following equations were used to calculate the concentration C (mmol·L^{-1}) of equilibrium chloride and the capacity W (mg·g^{-1}) of chloride adsorption at the equilibrium.

$$C = \frac{C_{AgNO_3} \times V_{AgNO_3}}{V_f} \quad (1)$$

$$W = \frac{35.45 \times V_0 \times (C_0 - C)}{m} \quad (2)$$

where C was the equilibrium chloride concentration (mmol·L^{-1}), C_{AgNO_3} was the concentration of $AgNO_3$ (mmol·L^{-1}) and V_{AgNO_3} was the volume of $AgNO_3$ (L). V_f was the volume of supernatant (L), W(mg·g^{-1}) was the chloride adsorption capacity at the equilibrium, V_0 was the total volume of simulated pore solution (L), C_0 was the chloride concentration of the solution before adsorption (mmol·L^{-1}) and m was the mass of MAL (g). Furthermore, a PHS-3E pH meter was used to measure the pH values of OPCH and SH after the addition of MAL.

2.2.4. Electrochemical Measurement

The steel specimens used were cylinders with a size of Φ10 mm × 5 mm. The bottom face of the steel was connected by a wire and the upper face was used as a corrosion face. The surface of the steel except the corrosion face was coated with epoxy. Some emery papers of 300, 600, 1200 and 2000 grades were applied to polish the corrosion face of the steel. Then, the steel specimens were degreased in acetone and washed with deionized water. After drying, the steel was put in the saturated calcium hydroxide solution for 7 d for the passivation treatment. Then, the steel was put in the solutions of SH, OPCH containing 3.5 wt.% NaCl. For evaluating the corrosion inhibition effects of MAL-N3 and MAL-N2, 1.0 wt.% MAL was added into the solutions. Electrochemical measurement was performed using the electrochemical workstation Parstat 2273 with three electrodes. The saturated calomel electrode (SCE) was used as the reference electrode. The platinum electrode (PE) was used as the auxiliary electrode. The steel was used as the working electrode. The corrosion potential (E_{corr}), the electrochemical impedance spectroscopy (EIS) and potentiodynamic polarization (PDP) of the steel specimens were measured. To measure EIS, a sinusoidal potential perturbation of ±10 mV was applied and its frequency range was from 10 mHz to 100 kHz. The range of scanning of PDP was from −250 mV versus E_{corr} to +800 mV and the scanning rate was 1 mV/s.

2.2.5. Structural Characterization

The morphology of the prepared MAL was obtained by the scanning electron microscope (SEM) of Zeiss Supra55 using an accelerating electric voltage of 15 kV. After electrochemical measurement, the optical microscope Olympus BHM was used to observe the surface morphology of the steel specimens. The X-ray diffractometer Bruker D8 advance with Cu Kα radiation (40 kV and 40 mA) at a scanning rate of 5°/min was used to obtain the X-ray diffraction (XRD) patterns of the MAL powder before and after chloride adsorption. The scanning range of XRD was 5~90°. Thermo Scientific Nicolet iS5 was applied to record the Fourier transform infrared (FT-IR) spectra of the MAL powder. The spectral range of the FT-IR was from 390 cm^{-1} to 4000 cm^{-1} and the number of scanning repetitions was 32 times.

3. Results and Discussion

3.1. Characterization of Synthesized MAL

The morphologies of MAL-C, MAL-0, MAL-N3 and MAL-N2 as well as the elemental compositions of MAL-N3 and MAL-N2 are shown in Figure 1. The layered structure of MAL-C with a size of 150~250 nm is observed in Figure 1a. The product MAL-0 after calcination is shown in Figure 1b. The layered structure collapses and its size is decreased to 100~220 nm. As shown in Figure 1c,d, the synthesized MAL-N3 and MAL-N2 present a hexagonal layered structure, which is a typical structure of layered double hydroxides (LDHs). The similar microstructure of LDHs has also been reported in the previous literature [20–22]. The difference in the size of the samples may be caused by the preparation method, or by the types of metal cations or intercalated anions. In the present work, the layered structure is restored with a size distribution of 250~400 nm and a thickness of 10 nm because of the structural reconstruction property of MAL. The

small layered structures are stacked into a three-dimensional network. Figure 1e,f show the element compositions of spot 1 and spot 2 on MAL-N3 and MAL-N2, respectively. According to the EDS spectra, the Mg:Al ratios of synthesized MAL-N3 and MAL-N2 are both approximately 2:1, which is in accord with the proportion of elements in the chemical formula of the raw material (MAL-C, $Mg_4Al_2(OH)_{12}CO_3 \cdot mH_2O$). Their N percentages are 4.6% and 5.1%, respectively. This indicates that NO_3^- and NO_2^- have been intercalated into the interlayer of MAL and that MAL-N3 and MAL-N2 have been successfully synthesized.

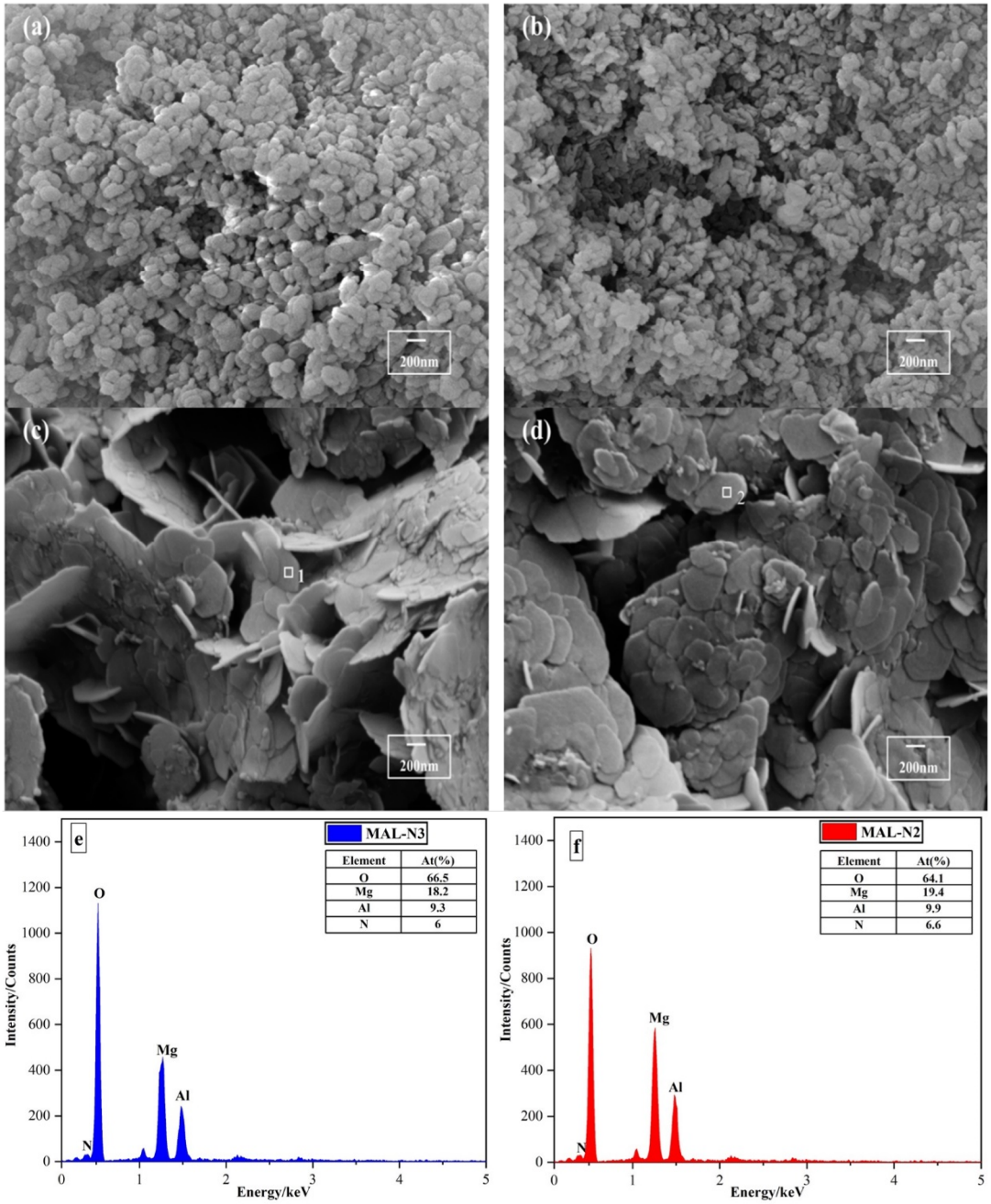

Figure 1. SEM micrographs of (**a**) MAL-C; (**b**) MAL-0; (**c**) MAL-N3; (**d**) MAL-N2 and EDS results of (**e**) spot 1 on MAL-N3; (**f**) spot 2 on MAL-N2.

3.2. Chloride Adsorption and the Change of pH Value

3.2.1. Chloride Adsorption Equilibrium Isotherms

Langmuir and Freundlich isotherm equations are used to fit the obtained data of chloride adsorption on MAL-N3 and MAL-N2 in OPCH and SH, respectively.

Langmuir isotherm equation:

$$W = \frac{K_l \cdot W_s \cdot C}{1 + K_l \cdot C} \tag{3}$$

Freundlich isotherm equation:

$$W = K_f \cdot C^n \tag{4}$$

where K_l is the adsorption rate constant, W_s is the saturated adsorption capacity ($mg \cdot g^{-1}$), W is the adsorption capacity ($mg \cdot g^{-1}$), C is the equilibrium chloride concentration ($mmol \cdot L^{-1}$), K_f is the constant related to the adsorption capacity, n is the adsorption constant and R^2 is the fitting correlation coefficient.

Figure 2 shows the Langmuir and Freundlich fitting curves of the chloride isotherm adsorption on MAL-N3 and MAL-N2 in OPCH and SH at room temperature. The fitting parameters K_f, K_l, W_s, n and R^2 are shown in Table 2. The Langmuir fitting correlation coefficients R^2_L of the chloride adsorption isotherms of MAL-N3 and MAL-N2 in OPCH and SH are higher than the Freundlich fitting correlation coefficients R^2_F. Therefore, the Langmuir isotherm is more suitable to fit the obtained data of chloride adsorption on MAL than the Freundlich isotherm. Compared to MAL-N2, the saturated chloride adsorption capacities of MAL-N3 in SH and OPCH are higher.

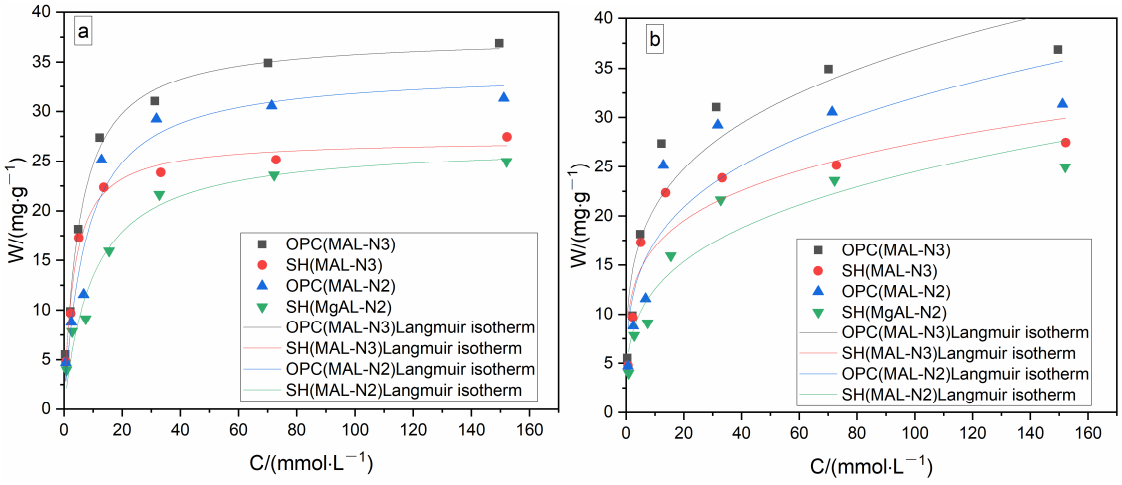

Figure 2. (**a**) Langmuir isotherm and (**b**) Freundlich isotherm of Cl^- adsorption on the MAL in OPCH and SH.

Table 2. Fitting parameters for chloride absorption isotherms of MAL in OPCH and SH.

MAL	Solution	Langmuir			Freundlich		
	Type	K_l/(L·mmol^{-1})	W_s/(mg·g^{-1})	R^2_L	K_f	n	R^2_F
MAL-N3	OPCH	0.191	37.601	0.985	11.845	0.246	0.876
MAL-N2	OPCH	0.133	34.189	0.936	9.443	0.265	0.789
MAL-N3	SH	0.295	27.156	0.986	10.379	0.210	0.818
MAL-N2	SH	0.099	26.858	0.960	6.434	0.290	0.891

This result may be related to the volume of intercalated anions [23]. Compared to MAL in OPCH, MAL in SH possesses a lower saturated chloride adsorption capacity. The

reason may be that the pH value of SH is higher than that of OPCH. Therefore, there are more OH^- in SH competing with Cl^- to exchange with anions NO_x [24]. Furthermore, the decrease in adsorption sites of MAL in SH makes the chloride adsorption capacity lower [25].

3.2.2. The Change of pH Value

After the addition of MAL in OPCH and SH, the pH values of OPCH and SH decrease. The changes of hydroxyl ion concentration ($[OH^-]$) in OPCH and SH in the presence of MAL are shown in Figure 3. The result indicates that MAL-N3 and MAL-N2 have pH buffer effects [26]. Furthermore, the $[OH^-]$ in OPCH and SH in the presence of MAL-N3 are more remarkably decreased compared to those in the presence of MAL-N2. The buffer effect may be ascribed to the exchange of OH^- with the anions in the galleries of MAL [27]. Meanwhile, the different decreases in $[OH^-]$ may be caused by the different competitive adsorption behaviors of OH^- with Cl^- on MAL-N3 and MAL-N2. The decreasing value of $[OH^-]$ in SH due to the additions of MAL-N3 and MAL-N2 are more prominent compared to those in OPCH, confirming the more dramatic competitive adsorption in SH.

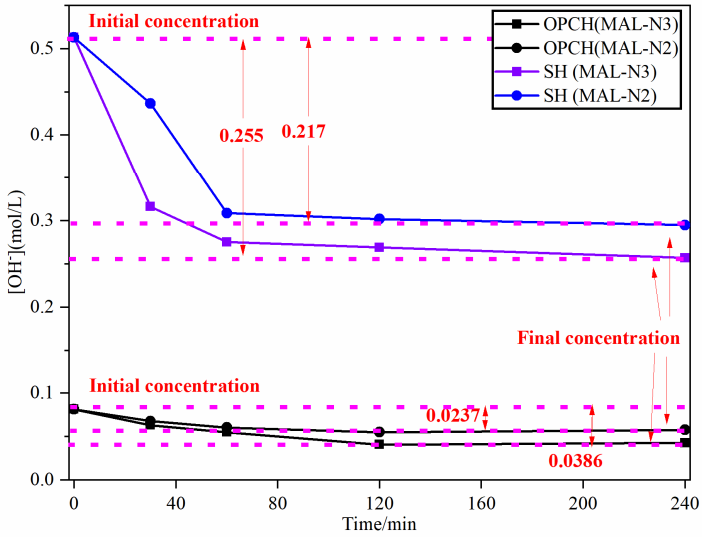

Figure 3. Variations of $[OH^-]$ in OPCH and SH containing chloride ions after the addition of MAL.

3.3. Corrosion Protection Performance

3.3.1. Corrosion Potential of Steel

The changes in corrosion potential of steel specimens in the simulated pore solutions with immersion time are shown in Figure 4. In OPCH, the corrosion potential of steel specimens decreases with the increase in immersion time due to the corrosion attack of aggressive Cl^- [28]. Compared to the steel specimen in OPCH in the absence of MAL, the potential of steel specimens in OPCH with the additions of MAL-N3 and MAL-N2 increases by 80 mV and 90 mV at the immersion time of 50 h, indicating that MAL has a corrosion inhibition effect. Initially, the steel specimen in OPCH in the presence of MAL-N3 has a more positive potential than that in the presence of MAL-N2, which may be mainly ascribed to the higher chloride adsorption capacity of MAL-N3. Although the chloride adsorption capacity of MAL-N2 is relatively lower, the released NO_2^- has a better corrosion inhibition effect because of its faster reduction than nitrate [29,30]. Then, the corrosion potential of steel specimens in OPCH in the presence of MAL-N2 becomes about 40 mV more positive than that in the presence of MAL-N3 after the immersion time of 50 h, indicating that MAL-N2 has a long-term corrosion inhibition effect in OPCH [31]. When MAL-N3 and MAL-N2 are added to SH, the steel specimens have more positive potential compared to those in OPCH, indicating that MAL has a better corrosion inhibition effect in SH than

OPCH. Furthermore, the potential of steel specimens in SH in the presence of MAL-N2 is about 100 mV more positive than that in the presence of MAL-N3, indicating that MAL-N2 has a better corrosion inhibition effect than MAL-N3 in SH.

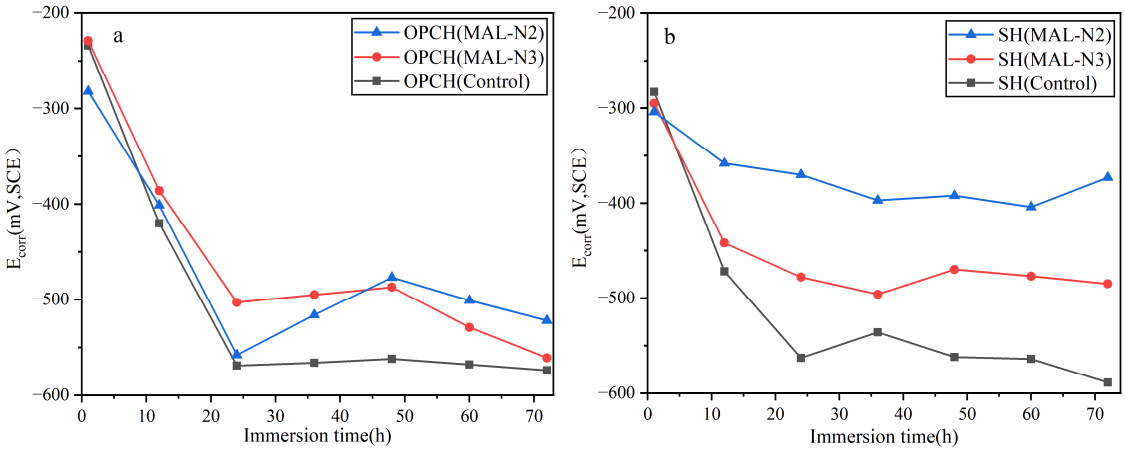

Figure 4. Variations of corrosion potential of the steel in (**a**) OPCH; (**b**) SH containing 3.5 wt.% NaCl after the addition of MAL.

3.3.2. Electrochemical Impedance Spectroscopy (EIS) Measurement

The EIS plots of steel specimens at different immersion times after adding MAL-N3 and MAL-N2 in OPCH and SH containing 3.5 wt.% NaCl are shown in Figure 5. All the impedance plots seem like semicircles. Initially, the impedance plots present a resistive behavior at high frequencies and later, on the impedance plots at low frequencies, change toward a capacitive behavior. In the Nyquist plot, Z'' is the imaginary part of impedance and Z' is the real part of impedance. $|Z|$ in the Bode diagram is the modulus of impedance. The radius of the capacitive arc is closely associated with the charge transfer resistance of the system. It is equivalent to the polarization resistance (R_p) of the steel specimen. The capacitive arc radius in the impedance plot for the steel specimens in the absence of MAL in OPCH shrinks with the increase in immersion time, indicating the gradual corrosion of the steel. The capacitive arc radiuses for the steel specimens with the additions of MAL-N3 and MAL-N2 in OPCH are bigger than those in the absence of MAL. Such a result indicates that MAL-N3 and MAL-N2 both have good corrosion inhibition effects in OPCH. Compared to the steel specimen in OPCH in the presence of MAL-N3, the steel specimen in OPCH in the presence of MAL-N2 has a larger radius of capacitive arc, indicating that MAL-N2 has a better corrosion inhibition effect in OPCH.

The Nyquist and Bode diagrams of the steel specimens in SH in the presence of MAL-N3 and MAL-N2 at different immersion times are shown in Figure 6. The capacitive arc radius in the impedance plot for the steel specimen in SH in the absence of MAL shrinks with the increase in immersion time. Furthermore, the capacitive arc radiuses for the steel specimens in SH in the presence of MAL are larger compared to those in the absence of MAL. Such a result indicates that MAL has an excellent corrosion inhibition effect in SH. Compared to the steel specimen in SH in the presence of MAL-N3, the steel specimen in SH in the presence of MAL-N2 has a larger capacitive arc radius, which is attributed to the better corrosion inhibition effect of NO_2^- in the interlayer of MAL-N2. This is consistent with the conclusion obtained from the corrosion potential of steel. Compared to the steel specimens in OPCH, the steel specimens in SH have larger capacitive arc radiuses. The reason for this may be that after the chloride adsorption by MAL, the pH value of SH is still higher than that of OPCH. The higher alkalinity results in a smaller ratio of $[Cl^-]/[OH^-]$ in SH, promoting the slower corrosion of the steel specimen in SH [32].

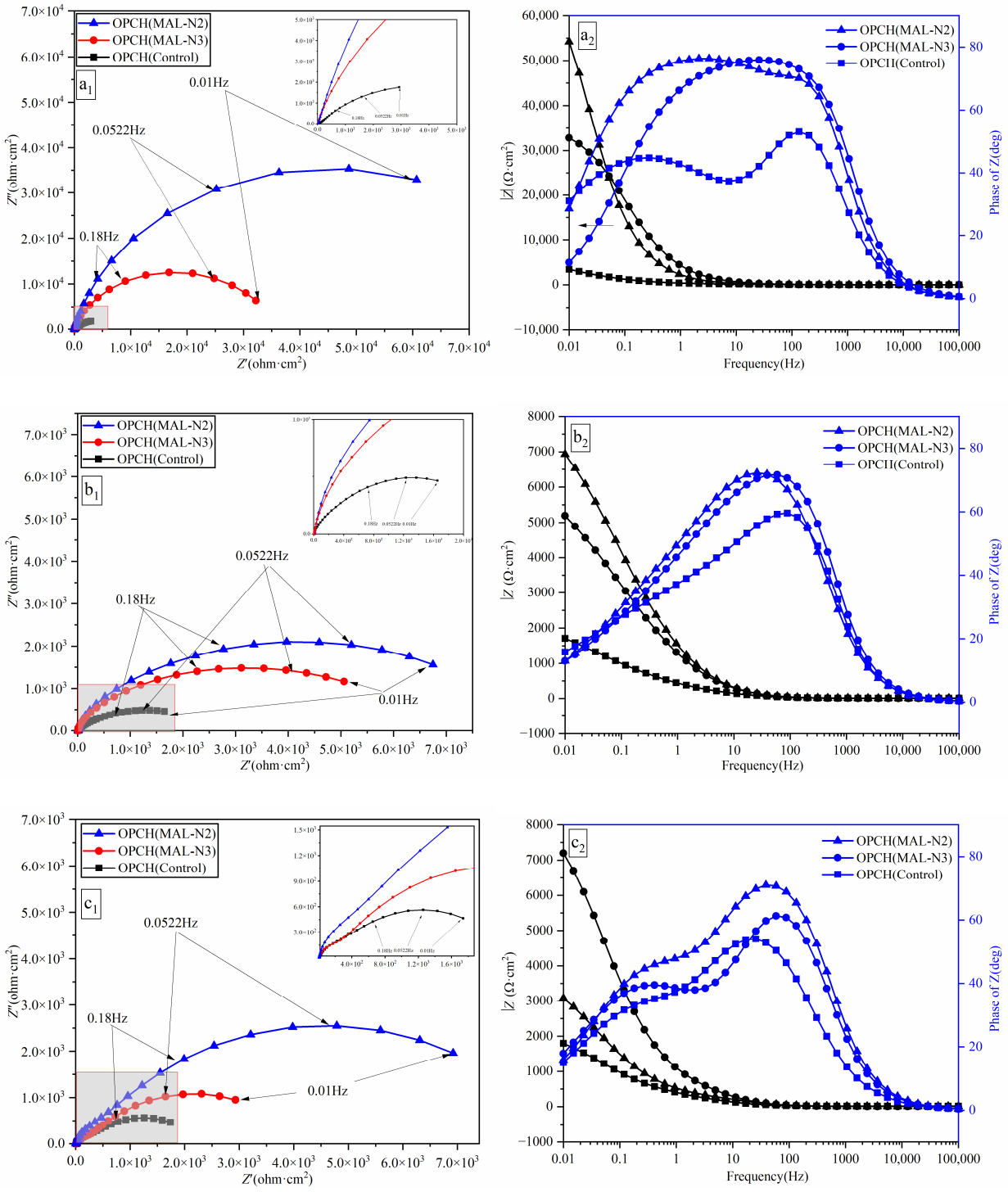

Figure 5. Nyquist diagrams and Bode diagrams of steel specimens in chloride-contaminated OPCH at ($\mathbf{a_1}$,$\mathbf{a_2}$) 24 h immersion time; ($\mathbf{b_1}$,$\mathbf{b_2}$) 48 h immersion time; ($\mathbf{c_1}$,$\mathbf{c_2}$) 72 h immersion time.

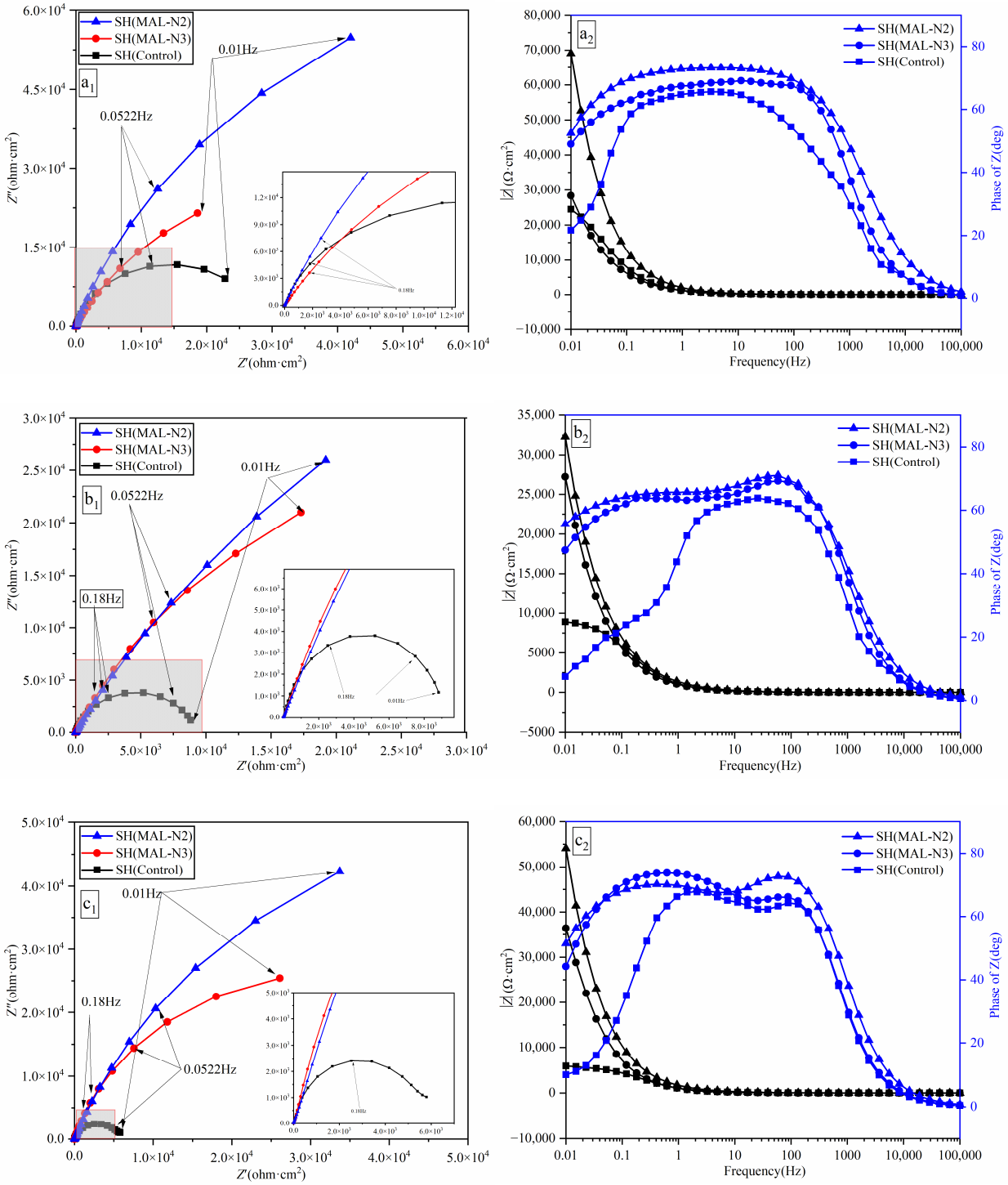

Figure 6. Nyquist diagrams and Bode diagrams of steel specimens in chloride-contaminated SH at (**a**$_1$,**a**$_2$) 24 h immersion time; (**b**$_1$,**b**$_2$) 48 h immersion time; (**c**$_1$,**c**$_2$) 72 h immersion time.

Zsimpwin software is used to fit the EIS plots and the equivalent circuits shown in Figure 7a,b are used for fitting. In the figure, R_s represents the electrolyte resistance, Q_1 is the film capacitance, R_1 is the film resistance, Q_2 is the double-layer capacitance, R_2 is charge transfer resistance of the steel specimen and W is the semi-infinite Warburg impedance, respectively. In the initial immersion time, the fitting error of equivalent circuit (a) R(Q(R(QR))) is very low. However, when the immersion time extends, the fitting error of equivalent circuit (a) R(Q(R(QR))) becomes higher. At this time, the equivalent circuit

(b) R(Q(R(Q(RW)))) is used for the fitting. The parameters obtained by fitting the EIS plots are shown in Table 3. R_s in SH obtained by fitting is smaller than R_s in OPCH because of more Na^+, K^+ cations in SH. A constant phase element (CPE) is used to express Q_1, Q_2, with the impedance Z_{cpe} defined by Equation (5).

$$Z_{cpe} = \frac{1}{Y_o \cdot (iw)^n} \tag{5}$$

where w is the angular frequency, Y_0 is the frequency-independent admittance and i is the imaginary number; the value n gives information on the nature of the CPE, being $n = 1$ for a pure capacitor and $n = 0.5$ for a mass transfer process. The effective capacitance can be calculated by the following equations [33]:

$$C^B = Y_0^{\frac{1}{n}} \cdot \left(\frac{1}{R_e} + \frac{1}{R_f} \right)^{\frac{n-1}{n}} \tag{6}$$

$$C^H = Y_0^{\frac{1}{n}} \cdot \left(\frac{1}{R_f} \right)^{\frac{n-1}{n}} \tag{7}$$

where R_e is the resistance in series with the CPE and R_f is the resistance in parallel with the CPE. The effective capacitances C_1, C_2 are calculated by Equation (6) or (7) and they are shown in Table 3.

The thickness of passive film d is calculated by the following equation:

$$d = \frac{\varepsilon_r \cdot \varepsilon_0 \cdot s}{C} \tag{8}$$

where ε_r is the relative dielectric constant, ε_0 is the vacuum dielectric constant and s is the effective working surface area. The effective capacitances C^B, C^H of the steel specimens in SH are lower compared with those in OPCH. Thus, the thickness of passive film of the steel specimen in SH is bigger than that in OPCH. The denser passive film may be attributed to the higher alkalinity of SH although the steel specimens are pre-passivated in the saturated calcium hydroxide solution. The presence of Warburg resistance means that corrosion products are deposited at the corrosion interface [34]. The steel corrosion will be hindered by the corrosion products, while the rate of corrosion is controlled by the diffusion of corrosion products.

Furthermore, the charge transfer resistances (R_2) of steel specimens with the additions of MAL-N3 and MAL-N2 in OPCH are higher compared with those in the absence of MAL, indicating that the corrosion rate of steel specimens with the additions of MAL-N3 and MAL-N2 in OPCH are relatively lower. Compared to the steel specimen in OPCH in the presence of MAL-N3, the steel specimen in OPCH in the presence of MAL-N2 has a higher R_2 value, confirming the better corrosion inhibition effect of MAL-N2 in OPCH. Moreover, the R_2 value for the steel specimen in SH in the presence of MAL-N2 is higher than that of the steel specimen in SH in the presence of MAL-N3, suggesting that the corrosion inhibition effect of MAL-N2 is better than MAL-N3 in SH. The reason for this may be that the released NO_2^- has a better corrosion inhibition effect than the released NO_3^- due to the anion exchange of LDH materials. Furthermore, MAL in SH increases the R_2 values of the steel specimens by a higher level than those in OPCH, suggesting that a higher alkalinity of the solution can affect the corrosion inhibition effect of MAL. The higher alkalinity of the solution leads to the decrease in threshold $[NO_x^-]/[Cl^-]$, which must be reached to hinder the steel corrosion by the inhibitive anions [35,36].

Table 3. Fitting parameters with the equivalent-circuit model for the steels in OPCH and SH.

Immersion Time/h	Solution Type	$R_s/(\Omega \cdot cm^{-2})$	$C_1^B/(\mu F \cdot cm^{-2})$	$C_1^H/(\mu F \cdot cm^{-2})$	n	$R_1/(\Omega \cdot cm^{-2})$	$C_2^B/(\mu F \cdot cm^{-2})$	$C_2^H/(\mu F \cdot cm^{-2})$	n	$R_2/(\Omega \cdot cm^{-2})$	$W/(\Omega \cdot cm^{-2})$
24	OPCH	9.62	27.79	36.01	0.91	110.80	221.99	3798.00	0.59	7090	
24	OPCH(MAL-N3)	9.43	7.63	9.38	0.93	104.30	4.41	41.16	0.71	33,800	
24	OPCH(MAL-N2)	7.98	2.74	38.67	0.80	177.50	13.43	78.42	0.78	92,260	
48	OPCH	7.49	5.80	8.20	0.80	21.52	316.33	1054.89	0.80	2641	
48	OPCH(MAL-N3)	8.46	12.31	14.61	0.89	25.29	3.90	324.25	0.56	6984	
48	OPCH(MAL-N2)	11.37	35.56	52.98	0.92	1103.00	53.36	368.00	0.52	7829	
72	OPCH	12.71	55.09	138.00	0.79	387.20	705.00	2180.00	0.61	1898	0.015900
72	OPCH(MAL-N3)	10.52	32.90	47.57	0.90	279.50	300.00	1468.00	0.63	3844	0.004470
72	OPCH(MAL-N2)	9.00	33.31	48.80	0.92	719.00	121.00	126.00	0.66	8179	0.002621
24	SH	5.29	31.32	41.23	0.92	148.10	54.30	137.50	0.85	28,550	
24	SH(MAL-N3)	5.86	29.37	44.98	0.90	308.10	42.40	543.70	0.69	91,410	
24	SH(MAL-N2)	4.02	21.14	61.77	0.83	799.80	24.70	15.47	0.61	197,920	
48	SH	4.99	38.36	44.89	0.95	132.70	61.30	121.66	0.86	9068	
48	SH(MAL-N3)	4.73	37.87	49.78	0.93	189.60	47.10	577.50	0.71	87,750	
48	SH(MAL-N2)	5.24	26.26	52.56	0.87	566.60	27.80	726.80	0.64	182,930	
72	SH	5.40	48.87	55.67	0.96	120.9	65.9	105	0.89	5300	0.004975
72	SH(MAL-N3)	5.46	45.76	57.43	0.94	163.5	49.6	226.11	0.80	67,750	
72	SH(MAL-N2)	5.82	30.37	42.11	0.93	524.1	29.6	219.02	0.74	152,270	

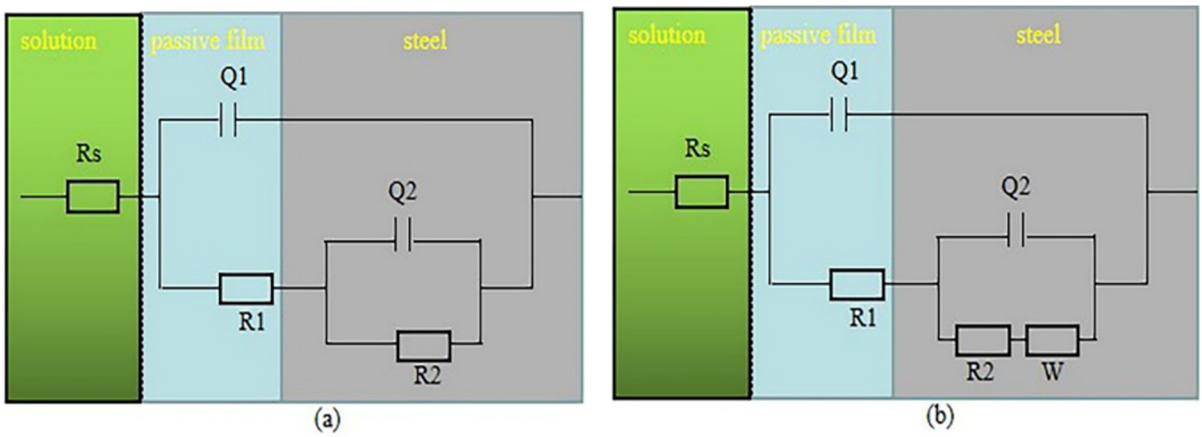

Figure 7. The equivalent-circuit models (**a**) R(Q(R(QR))); (**b**) R(Q(R(Q(RW)))) applied to analyze the EIS results of the steel.

3.3.3. Potentiodynamic Polarization

The potentiodynamic polarization curves of the steel specimens in OPCH and SH containing 3.5 wt.% NaCl at the immersion time of 72 h are shown in Figure 8. The electrochemical parameters, including corrosion potential (E_{corr}), corrosion current density (I_{corr}), cathodic Tafel slope (β_c) and anodic Tafel slope (β_a), are obtained through the extrapolation method from potentiodynamic polarization, as shown in Table 4. It can be seen that the corrosion potential of the steel specimen in OPCH in the presence of MAL-N3 is almost equal to that of the steel specimen in OPCH in the absence of MAL. In contrast, the addition of MAL-N2 increases the corrosion potential of the steel specimen by about 70 mV. Furthermore, the addition of MAL-N2 more obviously decreases the corrosion current density of steel than the addition of MAL-N3. Compared to the steel specimens with the additions of MAL-N3 and MAL-N2 in OPCH, the corrosion potential of the steel specimens with the additions of MAL-N3 and MAL-N2 in SH rises to more positive values. Also, the corrosion current densities decrease to lower values. To quantitatively determine the corrosion inhibition effect of MAL, it is required to calculate the corrosion inhibition efficiency (η). The corrosion inhibition efficiency (η) is calculated by the following Equation (9):

$$\eta = \frac{I_{corr,o} - I_{corr}}{I_{corr,o}} \quad (9)$$

where $I_{corr,o}$ is the corrosion current density of the steel specimen in the solution in the absence of MAL and I_{corr} is the corrosion current density of the steel specimen in the solution in the presence of MAL.

Table 4. Parameters obtained for the steels from potentiodynamic polarization curves in Figure 8.

Solution Type	MAL	E_{corr} (mV vs·SCE)	I_{corr} (μA·cm^{-2})	β_c (mV·dec^{-1})	β_a (mV·dec^{-1})	η (%)
OPCH	/	−706	18.600	98.5	616.4	/
	MAL-N3	−697	11.100	91.1	711.5	40.3
	MAL-N2	−637	1.870	67.8	249.1	89.9
SH	/	−601	3.370	96.1	419.6	/
	MAL-N3	−451	0.329	113.5	299.2	90.2
	MAL-N2	−329	0.169	124.8	388.2	94.9

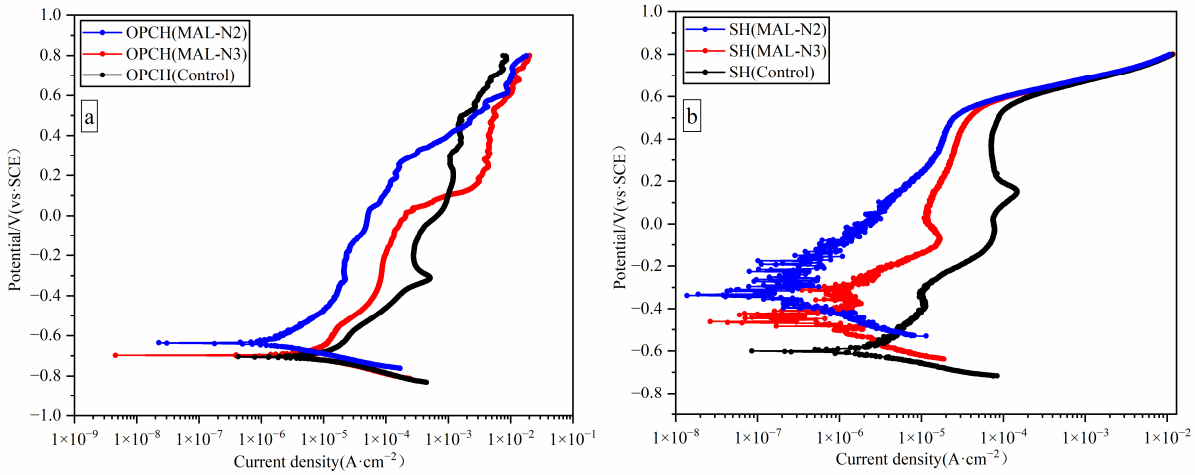

Figure 8. Potentiodynamic polarization curves of the steels in (**a**) OPCH; (**b**) SH containing 3.5 wt.% NaCl after adding MAL at the immersion time of 72 h.

Compared to MAL-N3 in OPCH, the corrosion inhibition efficiency of MAL-N3 in SH is significantly higher. Furthermore, the corrosion inhibition efficiency of MAL-N2 in SH is a little higher than that of MAL-N2 in OPCH. Furthermore, the corrosion inhibition efficiencies of MAL-N2 are higher than those of MAL-N3 in OPCH and SH.

3.3.4. Optical Micrographs

The optical micrographs of steel specimens before and after the immersion in OPCH and SH containing 3.5 wt.% NaCl are shown in Figure 9. Some corrosion pits can be clearly seen in Figure 9b, indicating that serious corrosion occurs on the steel specimen in OPCH. The number of corrosion pits on the surface of the steel specimen in OPCH slightly decreases after adding MAL-N3. In contrast, the number of corrosion pits significantly decreases after adding MAL-N2. The surface of the steel specimen in SH in the absence of MAL also has many corrosion pits. The number of corrosion pits significantly decreases when MAL-N3 is added in SH. There are almost no corrosion pits when MAL-N2 is added in SH. Accordingly, the corrosion inhibition effects of MAL-N2 are better than those of MAL-N3 in SH and OPCH. Such results are well consistent with the results obtained by the electrochemical measurements.

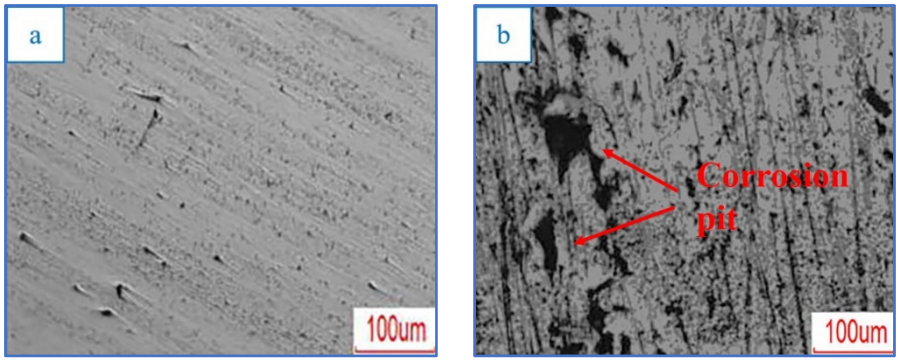

Figure 9. *Cont.*

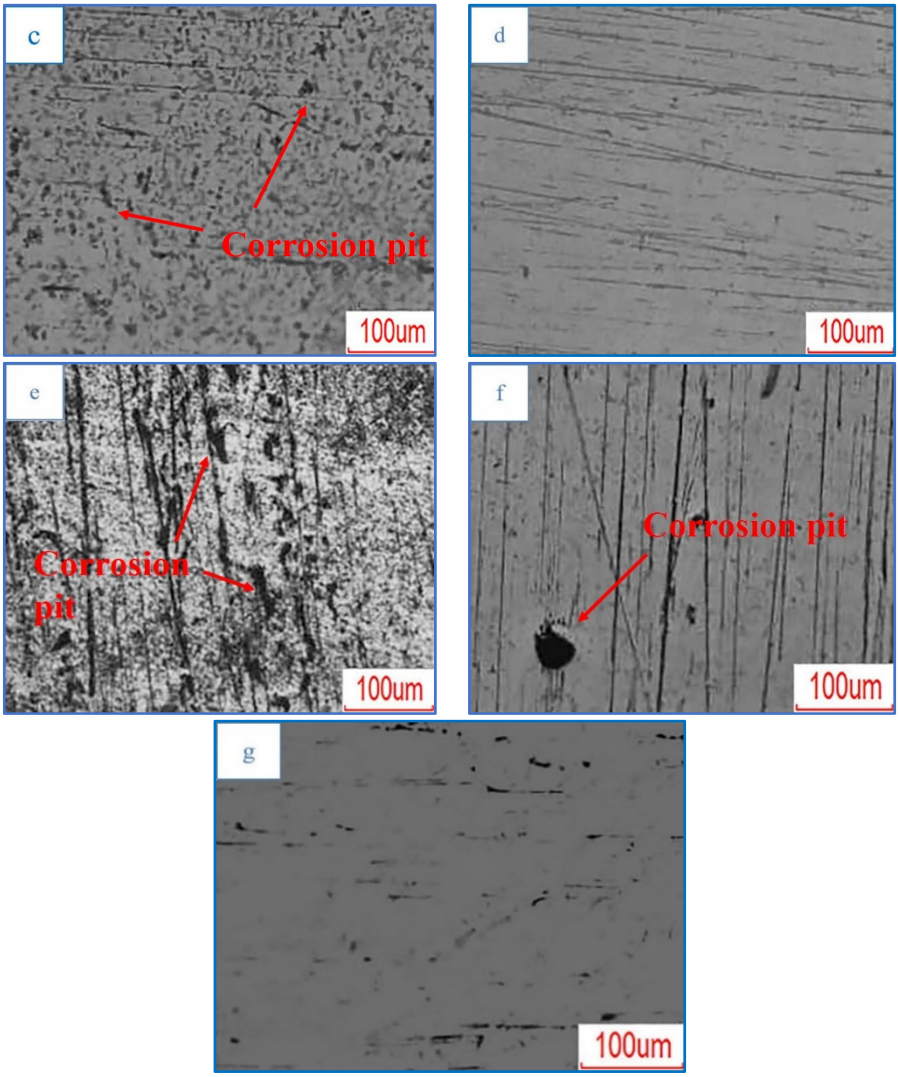

Figure 9. Optical micrographs of steel specimens before immersion (**a**); in absence of MAL (**b**); in presence of MAL-N3 (**c**) and MAL-N2 (**d**) in OPCH; in absence of MAL (**e**); in presence of MAL-N3 (**f**) and MAL-N2 (**g**) in SH.

3.4. Microstructure Characterization

The XRD patterns of MAL-N3 and MAL-N2 before and after Cl^- adsorption in OPCH and SH containing 160 mmol/L Cl^- are shown in Figure 10. Before Cl^- adsorption, the sharp diffraction reflections of MAL-N3 and MAL-N2 appear at 2θ angles of 11.47°, 23.26° and 34.91°and 11.63°, 23.36° and 34.89°. The sharp diffraction reflections indicate the well crystal forms of MAL-N3 and MAL-N2 [37]. Furthermore, the 2θ angles of diffraction reflections are consistent with the characteristics of MAL, which correspond to the (003), (006) and (009) planes. In SH and OPCH, the diffraction reflection intensities of MAL-N3 and MAL-N2 decrease after the Cl^- adsorption. Moreover, the 2θ angles of diffraction reflections corresponding to the (003) plane all increase to the higher values. According to the Brag equation, the basal space of MAL-N3 in OPCH after Cl^- adsorption decreases from 0.7741 nm to 0.7597 nm. Furthermore, the basal space of MAL-N3 in SH decreases to 0.7601 nm. The basal space of MAL-N2 in OPCH after Cl^- adsorption decreases from 0.7637 nm to 0.757 nm. Moreover, the basal space of MAL-N2 in SH decreases to 0.762 nm. The decrease in the basal spaces of MAL after Cl^- adsorption should be attributed to the replacements of NO_2^- and NO_3^- by Cl^- by means of the anion-exchange process.

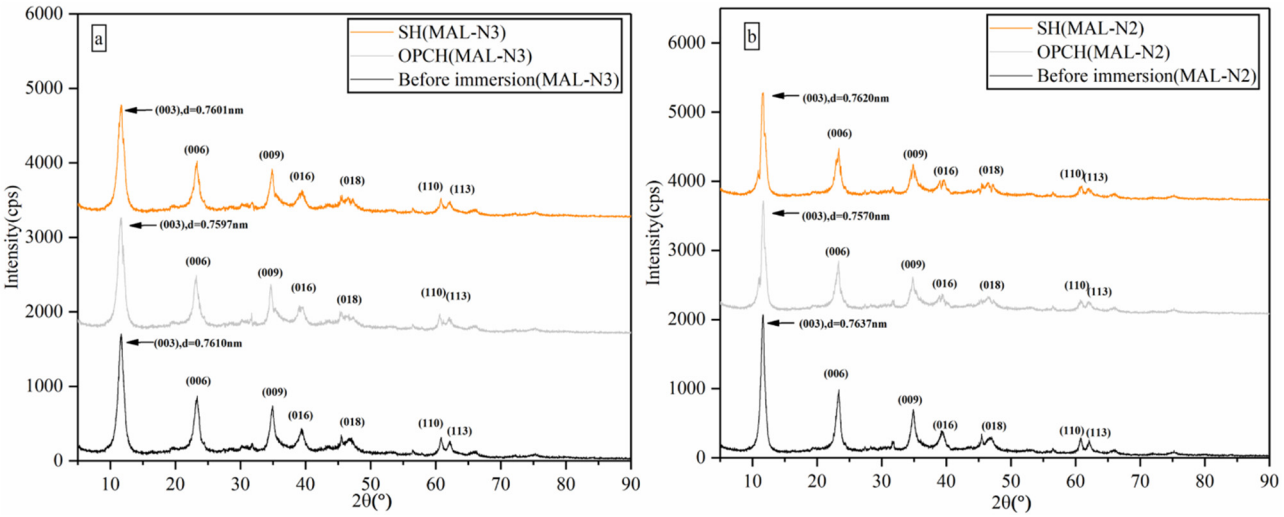

Figure 10. XRD patterns of (**a**) MAL-N3; (**b**) MAL-N2 in different simulated pore solutions after Cl^- adsorption.

The FT-IR spectra of MAL-N3 and MAL-N2 in OPCH and SH containing 160 mmol/L Cl^- are shown in Figure 11. Compared to OPCH, MAL in SH has a weaker band from 1633 cm^{-1} to 1271 cm^{-1}, which corresponds to the bending vibrations of H-OH. Furthermore, the intensities of the peak at 1382 cm^{-1} associated with the stretching vibrations of the nitrate group in MAL-N3 and the peak at 1366 cm^{-1} ascribed to the stretching vibrations of the nitrite group in MAL-N2 are relatively weaker. The reason for this may be that there are more OH^- in SH to exchange with NO_3^- and NO_2^-, resulting in a decrease in the number of nitrate groups and nitrite groups in the interlayer of MAL [38]. Moreover, the appearance of vibration of the nitrate group at 1366 cm^{-1} in the FT-IR spectra of MAL-N2 may be ascribed to the oxidation of nitrite during the synthesis process. After the adsorption of Cl^- in OPCH and SH, the intensity of the peak at 1382 cm^{-1} of MAL-N3 decreases. Furthermore, after the adsorption of Cl^- in OPCH and SH, the peak at 1271 cm^{-1} for MAL-N2 disappears. These results indicate the successful replacement of NO_3^- and NO_2^- with Cl^- after chloride adsorption.

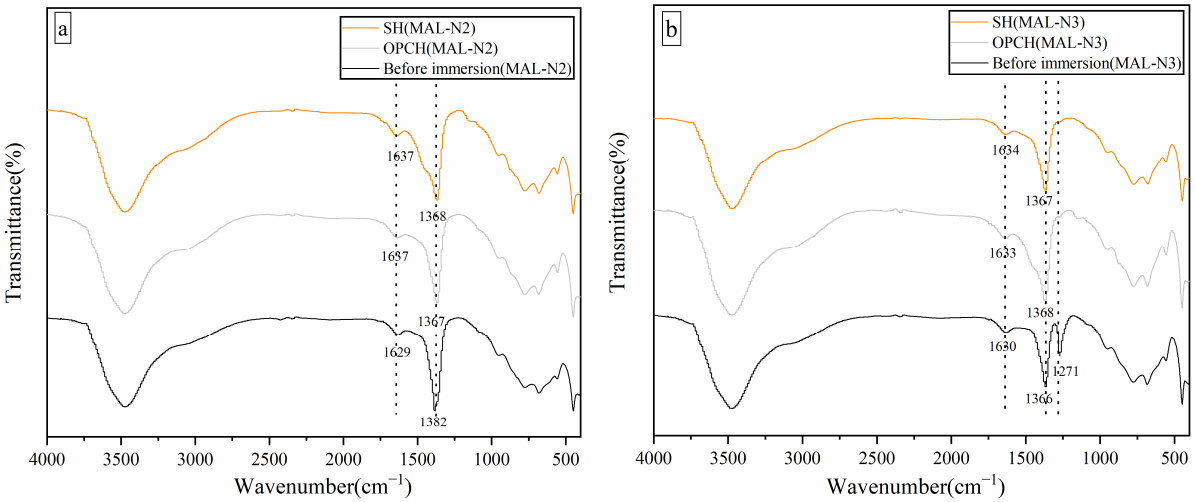

Figure 11. FT-IR spectra of (**a**) MAL-N3; (**b**) MAL-N2 in different simulated pore solutions after the Cl^- adsorption.

From the results obtained by the XRD and FT-IR measurements, it can be determined that the replacements of NO_2^- and NO_3^- by Cl^- in the gallery of MAL by means of the

anion-exchange process have happened after the immersion. Based on this, the amount of aggressive Cl^- in the corrosion solution is significantly reduced. Simultaneously, the NO_2^- and NO_3^- have been released to inhibit the steel corrosion. It is well known that the inhibitive ability of NO_2^- is better than NO_3^- in the alkaline solution. Moreover, owing to the competitive effect of OH^-, there are different chloride adsorption capacities and released NO_x^- in OPCH and SH. The different effects of MAL-N3 and MAL-N2 on the pH values of OPCH and SH also contribute to their corrosion inhibition.

4. Conclusions

(1) MAL-N3 and MAL-N2 have been successfully synthesized by the calcination rehydration method, presenting hexagonal layered structures with a size of 250~400 nm and a thickness of 10 nm, and they are stacked into a three-dimensional network. Furthermore, the synthesized MAL-N3 and MAL-N2 with a trigonal crystal system similar to brucite possess well crystal forms presented by sharp diffraction reflections in XRD patterns.

(2) MAL-N3 and MAL-N2 have lower chloride adsorption capacity in SH compared with that in OPCH. The Langmuir isotherm is more suitable to describe the chloride adsorption of MAL-N3 and MAL-N2 than the Freundlich isotherm. The chloride adsorption capacities of MAL-N3 in OPCH and SH are higher than those of MAL-N2. Due to the competitive adsorption between OH^- and Cl^-, the chloride adsorption capacity of MAL in SH with a higher pH value is lower than that in OPCH.

(3) Compared to MAL in simulated pore solution OPCH, MAL in SH has a better chloride-induced corrosion inhibition effect. Furthermore, the corrosion inhibition effect of MAL-N2 is superior to that of MAL-N3. The corrosion potentials of the steels in SH in the presence of MAL are more positive compared with those in OPCH. Furthermore, the corrosion potentials of the steels in solution in the presence of MAL-N2 have risen to more positive values compared to the steels with addition of MAL-N3. The polarization resistance of steel in SH in the presence of MAL is higher than that in OPCH; the result of potentiodynamic polarization indicates that the corrosion inhibition effect of MAL-N3 in SH is better than that in OPCH, while MAL-N2 in the two simulated pore solutions has a great corrosion inhibition effect.

(4) Different synergistic effects of NO_3^- and NO_2^- intercalated MAL in OPCH and SH contribute to the different corrosion inhibition effects. In XRD patterns, the decrease in d (003) value of MAL-N2 and MAL-N3 in OPCH and SH indicates the anion exchange between Cl^- and intercalated anion NO_2^-, NO_3^-. The peak at 1271 cm^{-1} of the FT-IR band of MAL-N2 disappears after Cl^- adsorption; furthermore, the intensity of the FT-IR band at 1382 cm^{-1} of MAL-N3 decreases, suggesting that intercalated NO_2^- and NO_3^- have been exchanged with Cl^-.

Author Contributions: Conceptualization, J.X. and Y.J.; formal analysis, Y.J.; investigation, M.Z., Y.J. and Y.W.; data curation, M.Z., Y.J. and Y.W.; writing—original draft preparation, M.Z., Y.J. and Y.W.; writing—review and editing, M.Z., Y.J. and Y.W.; supervision, Y.W.; project administration, J.X.; funding acquisition, J.X. All authors have read and agreed to the published version of the manuscript.

Funding: The authors gratefully acknowledge the financial support from The Key Research & Development Plan of Jiangsu Province, China (BE2021704).

Data Availability Statement: The raw data supporting the conclusions of this article will be made available by the authors on request.

Conflicts of Interest: The authors declare no conflicts of interest.

References

1. Matalkah, F.; Alomari, A.H.; Soroushian, P. Scaled-up production of alkali-activated cement in the presence of carbon dioxide for concrete construction. *Case Stud. Constr. Mater.* **2020**, *13*, e00463. [CrossRef]
2. Mozumder, R.A.; Laskar, A.I.; Hussain, M. Empirical approach for strength prediction of geopolymer stabilized clayey soil using support vector machines. *Constr. Build. Mater.* **2017**, *132*, 412–424. [CrossRef]

3. Laskar, S.M.; Mozumder, R.A.; Laskar, A.I. Behaviour of RC beam repaired using alkali activated slag-based agent under static and cyclic loading. *Structures* **2021**, *31*, 761–768. [CrossRef]
4. Nedeljkovic, M.; Lukovic, M.; van Breugel, K.; Hordijk, D.; Ey, G. Development and application of an environmentally friendly ductile alkali-activated composite. *J. Clean. Prod.* **2018**, *180*, 524–538. [CrossRef]
5. Liang, C.F.; Cai, Z.D.; Wu, H.X.; Xiao, J.Z.; Zhang, Y.M.; Ma, Z.M. Chloride transport and induced steel corrosion in recycled aggregate concrete: A review. *Constr. Build. Mater.* **2021**, *282*, 122547. [CrossRef]
6. Kenny, A.; Katz, A. Steel-concrete interface influence on chloride threshold for corrosion—Empirical reinforcement to theory. *Constr. Build. Mater.* **2020**, *244*, 118376. [CrossRef]
7. Mangat, P.S.; Ojedokun, O.O.; Lambert, P. Chloride-initiated corrosion in alkali activated reinforced concrete. *Cem. Concr. Compos.* **2021**, *115*, 103823. [CrossRef]
8. Shi, J.J.; Ming, J.; Wu, M. Passivation and corrosion behavior of 2304 duplex stainless steel in alkali-activated slag materials. *Cem. Concr. Compos.* **2020**, *108*, 103532. [CrossRef]
9. Ishizaki, T.; Chiba, S.; Watanabe, K.; Suzuki, H. Corrosion resistance of Mg-Al layered double hydroxide container-containing magnesium hydroxide films formed directly on magnesium alloy by chemical-free steam coating. *J. Mater. Chem. A* **2013**, *1*, 8968–8977. [CrossRef]
10. Hu, Y.R.; Li, H.H.; Wang, Q.; Zhang, J.; Song, Q. Characterization of LDHs prepared with different activity MgO and resisting Cl^- attack of concrete in salt lake brine. *Constr. Build. Mater.* **2019**, *229*, 116921. [CrossRef]
11. Tatematsu, H.; Sasaki, T. Repair materials system for chloride-induced corrosion of reinforcing bars. *Cem. Concr. Compos.* **2003**, *25*, 123–129. [CrossRef]
12. Shui, Z.H.; Ma, J.T.; Chen, W.; Chen, X.X. Chloride Binding Capacity of Cement Paste Containing Layered Double Hydroxide (LDH). *J. Test. Eval.* **2012**, *40*, 796–800. [CrossRef]
13. Geng, J.; Pan, C.G.; Wang, Y.; Chen, W.; Zhu, Y.Y. Chloride binding in cement paste with calcined Mg-Al-CO_3 LDH (CLDH) under different conditions. *Constr. Build. Mater.* **2021**, *273*, 121678. [CrossRef]
14. Xu, J.X.; Song, Y.B.; Zhao, Y.H.; Jiang, L.H.; Mei, Y.J.; Chen, P. Chloride removal and corrosion inhibitions of nitrate, nitrite-intercalated Mg-Al layered double hydroxides on steel in saturated calcium hydroxide solution. *Appl. Clay Sci.* **2018**, *163*, 129–136. [CrossRef]
15. Kayali, O.; Khan, M.S.H.; Ahmed, M.S. The role of hydrotalcite in chloride binding and corrosion protection in concretes with ground granulated blast furnace slag. *Cem. Concr. Compos.* **2012**, *34*, 936–945. [CrossRef]
16. Liu, T.; Chen, Y.X.; Yu, Q.L.; Fan, J.F.; Brouwers, H.J.H. Effect of MgO, Mg-Al-NO_3 LDH and calcined LDH-CO_3 on chloride resistance of alkali activated fly ash and slag blends. *Constr. Build. Mater.* **2020**, *250*, 118865. [CrossRef]
17. Xu, J.X.; Wei, J.F.; Ma, G.X.; Tan, Q.P. Effect of MgAl-NO_2 LDHs inhibitor on steel corrosion in chloride-free and contaminated simulated carbonated concrete pore solutions. *Corros. Sci.* **2020**, *176*, 108940. [CrossRef]
18. Cao, Y.H.; Dong, S.G.; Zheng, D.J.; Wang, J.J.; Zhang, X.J.; Du, R.G.; Song, G.L.; Lin, C.J. Multifunctional inhibition based on layered double hydroxides to comprehensively control corrosion of carbon steel in concrete. *Corros. Sci.* **2017**, *126*, 166–179. [CrossRef]
19. Yu, X.; Jiang, L.H.; Xu, J.X.; Zu, Y.H. Effect of Na2SiO3 content on passivation and corrosion behaviour of steel in a simulated pore solution of Na_2SiO_3-activated slag. *Constr. Build. Mater.* **2017**, *146*, 156–164. [CrossRef]
20. Zuo, J.; Wu, B.; Luo, C.; Dong, B.; Xing, F. Preparation of MgAl layered double hydroxides intercalated with nitrite ions and corrosion protection of steel bars in simulated carbonated concrete pore solution. *Corros. Sci.* **2019**, *152*, 120–129. [CrossRef]
21. Li, J.; Luo, M.; Chen, Z.; Zhuang, E.; Yu, B.; Chen, Y.; Nong, Y. Anti-corrosion mechanism of MgAl-LDHs inhibitors with varying anionic charge on reinforcing steel in simulated concrete pore solutions. *Constr. Build. Mater.* **2023**, *363*, 129882. [CrossRef]
22. Liu, A.; Tian, H.; Li, W.; Wang, W.; Gao, X.; Han, P.; Ding, R. Delamination and self-assembly of layered double hydroxides for enhanced loading capacity and corrosion protection performance. *Appl. Surf. Sci.* **2018**, *462*, 175–186. [CrossRef]
23. Xu, J.X.; Tan, Q.P.; Mei, Y.J. Corrosion protection of steel by Mg-Al layered double hydroxides in simulated concrete pore solution: Effect of SO_4^{2-}. *Corros. Sci.* **2020**, *163*, 108223. [CrossRef]
24. Malherbe, F.; Forano, C.; Besse, J.P. Use of organic media to modify the surface and porosity properties of hydrotalcite-like compounds. *Microporous Mater.* **1997**, *10*, 67–84. [CrossRef]
25. Fang, X.; Chen, C.; Jia, H.; Li, Y.N.; Liu, J.; Wang, Y.S.; Song, Y.L.; Du, T.; Liu, L.Y. Progress in Adsorption-Enhanced Hydrogenation of CO_2 on Layered Double Hydroxide (LDH) Derived Catalysts. *J. Ind. Eng. Chem.* **2021**, *95*, 16–27. [CrossRef]
26. Chubar, N.; Gilmour, R.; Gerda, V.; Micusík, M.; Omastova, M.; Heister, K.; Man, P.; Fraissard, J.; Zaitsev, V. Layered double hydroxides as the next generation inorganic anion exchangers: Synthetic methods versus applicability. *Adv. Colloid Interface Sci.* **2017**, *245*, 62–80. [CrossRef]
27. Miyata, S. Anion-exchange properties of hydrotalcite-like compounds. *Clays Clay Miner.* **1983**, *31*, 305–311. [CrossRef]
28. Macdonald, D.D.; Qiu, J.; Zhu, Y.K.; Yang, J.; Engelhardt, G.R.; Sagues, A. Corrosion of rebar in concrete. Part I: Calculation of the corrosion potential in the passive state. *Corros. Sci.* **2020**, *177*, 109018. [CrossRef]
29. Soylev, T.A.; Richardson, M.G. Corrosion inhibitors for steel in concrete: State-of-the-art report. *Constr. Build. Mater.* **2008**, *22*, 609–622. [CrossRef]
30. Li, X.J.; Gui, F.; Cong, H.B.; Brossia, C.S.; Frankel, G.S. Evaluation of Nitrate and Nitrite Reduction Kinetics Related to Liquid-Air-Interface Corrosion. *Electrochim. Acta* **2014**, *117*, 299–309. [CrossRef]

31. Rivera-Corral, J.O.; Fajardo, G.; Arliguie, G.; Orozco-Cruz, R.; Deby, F.; Valdez, P. Corrosion behavior of steel reinforcement bars embedded in concrete exposed to chlorides: Effect of surface finish. *Constr. Build. Mater.* **2017**, *147*, 815–826. [CrossRef]
32. Mu, J.; Li, Y.Z.; Wang, X. Crevice corrosion behavior of X70 steel in NaCl solution with different pH. *Corros. Sci.* **2021**, *182*, 109310. [CrossRef]
33. Hirschorn, B.; Orazem, M.E.; Tribollet, B.; Vivier, V.; Frateur, I.; Musiani, M. Determination of effective capacitance and film thickness from constant-phase-element parameters. *Electrochim. Acta* **2010**, *55*, 6218–6227. [CrossRef]
34. Kumar, H.; Yadav, V. Musa acuminata (Green Corrosion Inhibitor) as anti-pit and anti-cracking agent for Mild Steel in 5.0 M Hydrochloric Acid Solution. *Chem. Data Collect.* **2020**, *29*, 100500. [CrossRef]
35. Garces, P.; Saura, P.; Zornoza, E.; Andrade, C. Influence of pH on the nitrite corrosion inhibition of reinforcing steel in simulated concrete pore solution. *Corros. Sci.* **2011**, *53*, 3991–4000. [CrossRef]
36. Gonzalez, J.A.; Ramirez, E.; Bautista, A. Protection of steel embedded in chloride-containing concrete by means of inhibitors. *Cem. Concr. Res.* **1998**, *28*, 577–589. [CrossRef]
37. Bouali, A.C.; Iuzviuk, M.H.; Serdechnova, M.; Yasakau, K.A.; Wieland, D.C.F.; Dovzhenko, G.; Maltanava, H.; Zobkalo, I.A.; Ferreira, M.G.S.; Zheludkevich, M.L. Zn-Al LDH growth on AA2024 and zinc and their intercalation with chloride: Comparison of crystal structure and kinetics. *Appl. Surf. Sci.* **2020**, *501*, 144027. [CrossRef]
38. Huang, Z.H.; Sun, X.Y.; Li, Y.; Ge, W.; Wang, J.D. Adsorption behaviors of chitosan and the analysis of FTIR spectra. *Spectrosc. Spectr. Anal.* **2005**, *25*, 698–700.